Cellulose (2022) 29:557–569
https://doi.org/10.1007/s10570-021-04310-x

ORIGINAL RESEARCH

Dynamic crack initiation and growth in cellulose nanopaper

Chengyun Miao · Haishun Du · Xinyu Zhang · Hareesh V. Tippur

Received: 11 June 2021 / Accepted: 1 November 2021 / Published online: 22 November 2021

Abstract Cellulose nanopaper (CNP) made of cellulose nanofibrils has gained extensive attention in recent years for its lightweight and superior mechanical properties alongside sustainable and green attributes. The mechanical characterization studies on CNP at the moment have generally been limited to tension tests. In fact, thus far there has not been any report on crack initiation and growth behavior, especially under dynamic loading conditions. In this work, crack initiation and growth in self-assembled CNP, made from filtration of CNF suspension, are studied using a full-field optical method. Dynamic crack initiation and growth behaviors and time-resolved fracture parameters are quantified using Digital Image Correlation technique. The challenge associated with dynamic loading of a thin strip of CNP has been overcome by an acrylic holder with a wide pre-cut slot bridged by edge-cracked CNP. The ultrahigh-speed digital photography is implemented to map in-plane deformations during pre- and post-crack initiation regimes including dynamic crack growth. Under stress wave loading conditions, macro-scale crack growth occurs at surprisingly high-speed (600–700 m/s) in this microscopically fibrous material. The measured displacement fields from dynamic loading conditions are analyzed to extract stress intensity factors (SIF) and energy release rate (G) histories. The results show that the SIF at crack initiation is in the range of 6–7 MPa $m^{1/2}$, far superior to many engineering plastics. Furthermore, the measured values increase during crack propagation under both low- and high-strain rates, demonstrating superior fracture resistance of CNP valuable for many structural applications.

Supplementary Information The online version contains supplementary material available at https://doi.org/10.1007/s10570-021-04310-x.

C. Miao (✉) · H. V. Tippur
Department of Mechanical Engineering, Auburn University, Auburn, AL 36849, USA
e-mail: czm0048@auburn.edu

H. Du · X. Zhang
Department of Chemical Engineering, Auburn University, Auburn, AL 36849, USA

Graphical abstract

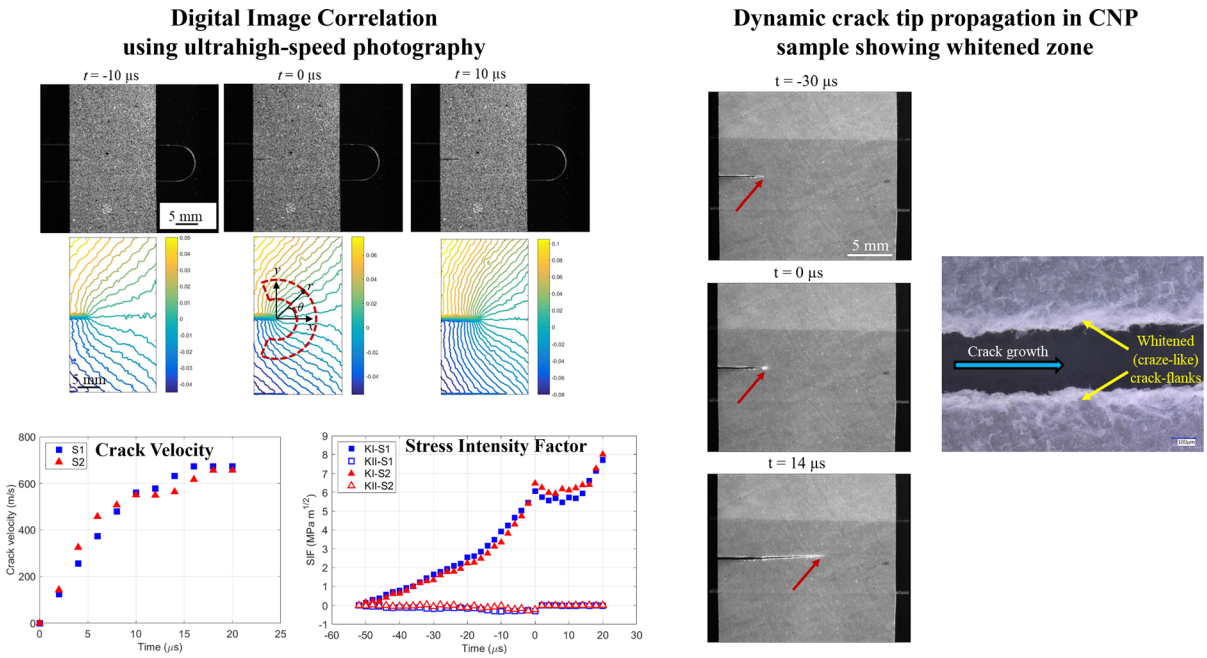

Keywords Cellulose nanopaper · Crack initiation and growth · Dynamic fracture · Ultrahigh-speed photography · Digital image correlation

Introduction

Cellulose nanofibrils (CNFs), an advanced bio-nanomaterial produced from lignocellulosic biomass, offer outstanding properties such as high elastic modulus (29–36 GPa), high specific surface area (up to several hundreds of m^2/g), high thermal stability (being stable against temperatures up to 300 °C), as well as biocompatibility, biodegradability and lightweight characteristics (Xie et al. 2018; Du et al. 2020). Therefore, CNFs possess great engineering potential in the fields of biomedical implants (Du et al. 2019; Liu et al. 2020), reinforcing nanofillers for structural composites (Lee et al. 2014; Kargarzadeh et al. 2018; Chen et al. 2020), packaging materials (Wu et al. 2020b; Du et al. 2021), energy storage devices (Liu et al. 2021; Du et al. 2022), optical and electro-conductive materials (Parit et al. 2020; Wu et al. 2020a), and so forth. Due to large specific surface area, high aspect ratio and semi-crystalline structure, CNFs exhibit remarkable tendency to entangle and form flexible and mechanically stable film or sheet, often referred to as cellulose nanopaper (CNP) (Benítez and Walther 2017). In addition to excellent mechanical properties, CNP also offers high thermal durability, tunable optical properties, as well as low thermal expansion coefficient (Wang et al. 2018). These make it a promising lightweight material for various multifunctional and high-end applications such as visual display substrates (Jung et al. 2015), organic solar cells (Nogi et al. 2015), and electrodes for energy storage (Xing et al. 2019).

A few results on the fracture behavior of CNP are reported in recent years. Zhu et al. (Zhu et al. 2015) found that the crack initiation toughness of CNP increased with the tensile strength. Using atomistic simulation, they attributed this to breaking and re-formation of hydrogen bonds among CNFs at crack initiation. Mao et al. (Mao et al. 2017) performed a comparative investigation of the fracture mechanisms of CNP, conventional printing paper, and Bucky paper and showed that both fiber pull-out and inter-fiber interactions play an important role in CNP behavior. Meng et al. (Meng et al. 2017, 2018) studied the effects of bridging of nanofibrils on the macroscale fracture toughness of CNP. Miao et al. (Miao et al.

2020) comparatively evaluated crack initiation and growth behaviors of CNP made by two methods namely casting and filtration, and observed increasing crack growth resistance during the entire fracture process starting from crack initiation to significant growth. Their results also showed that the CNP made by the filtration method outperformed the cast counterpart in terms of mechanical properties. All the reported works on fracture of CNP to date, however, have primarily focused on quasi-static fracture. The possibility of re-formation of hydrogen bonds as well as observed craze-like features along the crack flanks due to crack growth in this three-dimensionally entangled nanofibrous material rises the possibility of loading rate dependent fracture behavior. Thus, a comprehensive fracture performance assessment of CNP, however, should include evaluation of both static and dynamic fracture characteristics. In fact, it is well-known that fracture of polymer-based composites with fibrous constituents such as the conventional fiber reinforced polymer composites (Lee et al. 2010; Miao and Tippur 2019) and CNF hydrogel composites (Yang et al. 2019) are strain rate dependent. Accordingly, the rate dependence of filtered CNP is explored in this work to bridge this gap.

The full-field optical techniques are particularly suitable for investigating fracture mechanics of CNP. Among the various options available in this regard, Digital Image Correlation (DIC) technique offers many advantages such as non-contact full-field quantification of deformations in the region-of-interest (ROI) and simplicity of implementation using recorded intensities/gray scales to quantify deformations (Chu et al. 1985). Some researchers have applied DIC to measure thermal expansion of cellulose nanocrystal (CNC) films (Diaz et al. 2013), the in-plane strain fields on CNP under tension (Zhao et al. 2018), and fracture strength of CNF hydrogel composite subjected to cyclic loading (Wyss et al. 2018).

This paper is aimed at exploring the dynamic fracture mechanics of CNP. The steps for preparing CNP is described first. The details about the experiments pertaining to mapping crack tip fields in single edge notched CNP specimens subjected to dynamic loadings by DIC are discussed next. This is followed by calculating fracture mechanics parameters (crack velocity, stress intensity factors and energy release rates) from the DIC measurements. Finally, fracture mechanics parameters are qualitatively correlated with fractographic features and summarized.

Experimental details

Preparation of CNP

The CNF aqueous gel at a concentration of around 3 wt.% was obtained from University of Maine, USA. As noted earlier, the CNP produced for this work was made by a standard *filtration method* (Parit et al. 2018) and the resulting material was accordingly termed F-CNP. The detailed procedures for the preparation of the F-CNP can be found in the previous work (Miao et al. 2020). The final F-CNP had a thickness of 40 ± 3 μm, and density of 1225 kg/m^3. As shown in Fig. 1, the morphology of the cross-section of the F-CNPs indicates that highly fibrous CNFs tightly entangled with each other due to strong hydrogen bonding. These abundant hydrogen bonds could contribute to mechanical strength and fracture characteristics of as-prepared F-CNP. The Young's modulus was 10.8 ± 0.3 GPa and Poisson's ratio was 0.23 ± 0.04; both these elastic properties were measured separately by performing uniaxial tension tests on F-CNP strips discussed elsewhere (Miao et al. 2020).

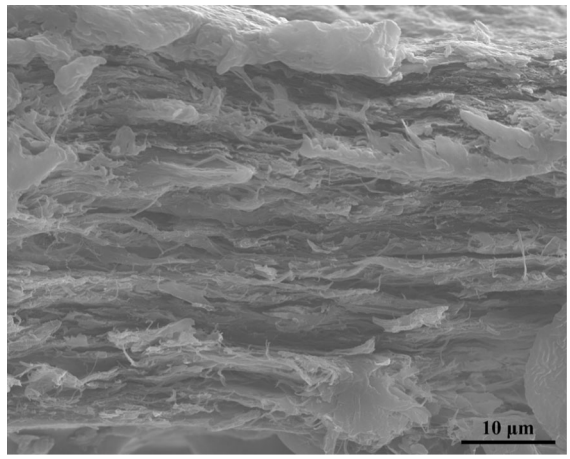

Fig. 1 SEM image showing typical cross-section of F-CNP

Dynamic fracture

The dynamic fracture behavior of F-CNP was investigated using DIC along with ultrahigh-speed photography. Single edge notched (SEN) specimens of dimensions 110 mm × 20 mm were prepared, and an initial notch of 5 mm length was cut into each of the samples using a sharp razor blade. The resulting crack tip had a root radius of 20–30 µm. To enable high-strain rate loading of F-CNP in mode-I conditions, a special specimen holder was devised. The holder consisted of a large acrylic (PMMA) support fixture (150 mm × 70 mm × 8.6 mm), as shown in Fig. 2, to which the specimen was adhered. The acrylic holder had a symmetric 40°V-notch cut into the middle of the edge of the holder and the V-notch flanks were extended into the holder as a relatively wide slot (approx. 10 mm wide) with a semicircular tip, as shown. To this holder, the F-CNP specimen was glued directly. The specimen was sprayed lightly with random black and white speckles to implement DIC (Chu et al. 1985) and map surface deformations. (The details of the method are intentionally avoided for brevity and can be found in a number of recent articles and monographs Yoneyama et al. 2006; Kirugulige et al. 2007; Sutton et al. 2009; Pan et al. 2009). The entire F-CNP specimen and the acrylic holder assembly was subjected to dynamic stress-wave loading along the flanks of the V-notch using a precisely matching wedge of a modified Hopkinson bar setup. The V-notch and the wide slot in the holder facilitated rapid tensile loading of the pre-notched F-CNP specimen causing it to fracture well before the failure of the holder.

The schematic of the experimental setup is shown in Fig. 3. A modified Hopkinson pressure bar was used to impact the acrylic holder to indirectly load the edge notched CNP specimen attached to the holder. The long-bar was 1.83 m long and 25.4 mm in diameter aluminum rod. The tip of the long-bar was machined and polished to be of a wedge-shape to match the V-notch in the acrylic holder. A 305 mm long, 25.4 mm diameter aluminum striker placed in the barrel of a gas-gun was launched towards the long-bar at a velocity of approx. 13 m/s during fracture tests. The compressive stress wave generated by the impact between the striker and the long-bar propagated the length of the long-bar before loading the specimen holder and then the F-CNP specimen. A close-up view of the optical setup is also shown in Fig. 3. Initially, the long-bar tip was kept in contact with the holder such that the V-notch flanks touched the long-bar. The

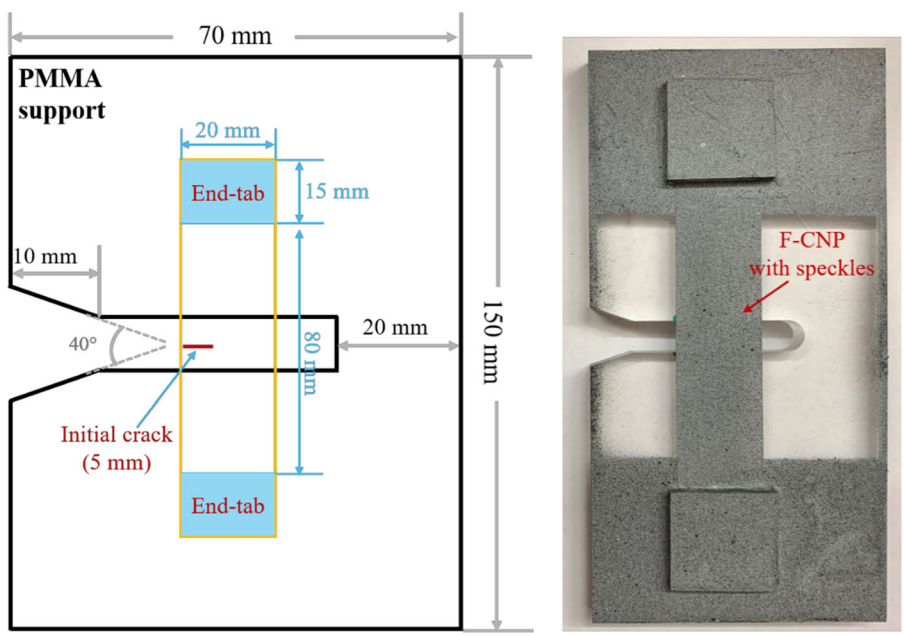

Fig. 2 Specimen geometry and loading configuration used for dynamic fracture tests: (left) schematic of specially designed PMMA support; (right) specimen assembly coated with random black and white speckles

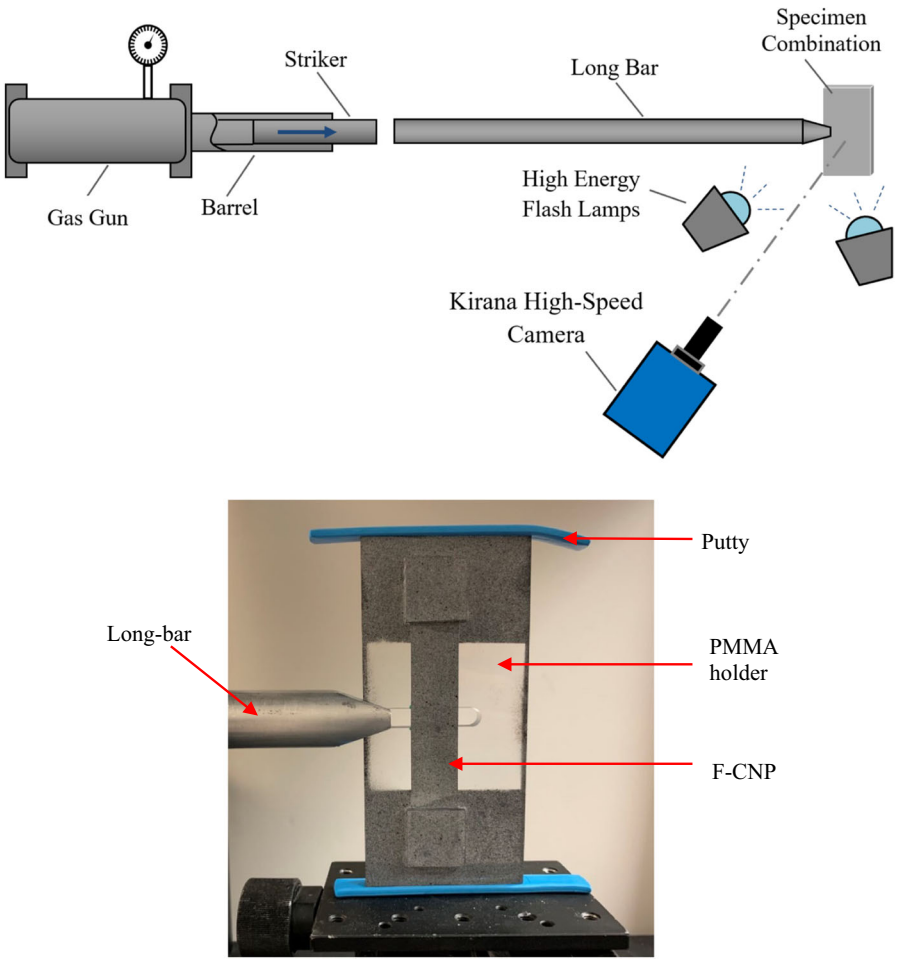

Fig. 3 Schematic (top) and close-up photograph (bottom) of the experimental setup used to study dynamic fracture of F-CNP

specimen holder was placed over a ∼1.5 mm thick rectangular soft putty strip on a platform with another identical putty strip pressed onto the top edge of the holder to achieve symmetry in terms of the acoustic impedance relative to the loading axis. The speckle images of the specimen illuminated by a pair of high energy flash lamps were recorded by a Kirana-05 M ultrahigh-speed digital camera at 500,000 frames per second (inter frame period 2 μs). When the striker impacted the long-bar, a trigger pulse was generated to start the recording of the speckle images by the camera with an adjustable/preset delay. The speckle images were subsequently analyzed using ARAMIS® image analysis software to extract in-plane displacement components, $u(x, y)$ and $v(x, y)$ in the x- and y-directions, respectively. During analysis, the speckle images were segmented into facets of size of 30 × 30 pixels (1 pixel = ∼44 μm on the specimen plane) with 25 pixels overlap which resulted in approx. 20 × 35 mm^2 region-of-interest (ROI).

The time-resolved speckle images along with the corresponding crack-opening displacements around a dynamically loaded mode-I crack in the F-CNP specimen are shown in Fig. 4 at a few select time instants (please see "Supplementary materials" for video). In these plots, $t = 0\mu s$ corresponds to one frame just before crack initiation at the original crack-tip, and color bars represent displacements in millimeters. It can be observed that, due to the symmetric nature of mode-I fracture, the crack propagated self-similarly along a horizontal path (from left to right in these images) and hence the contours of the two orthogonal displacements are highly symmetric in

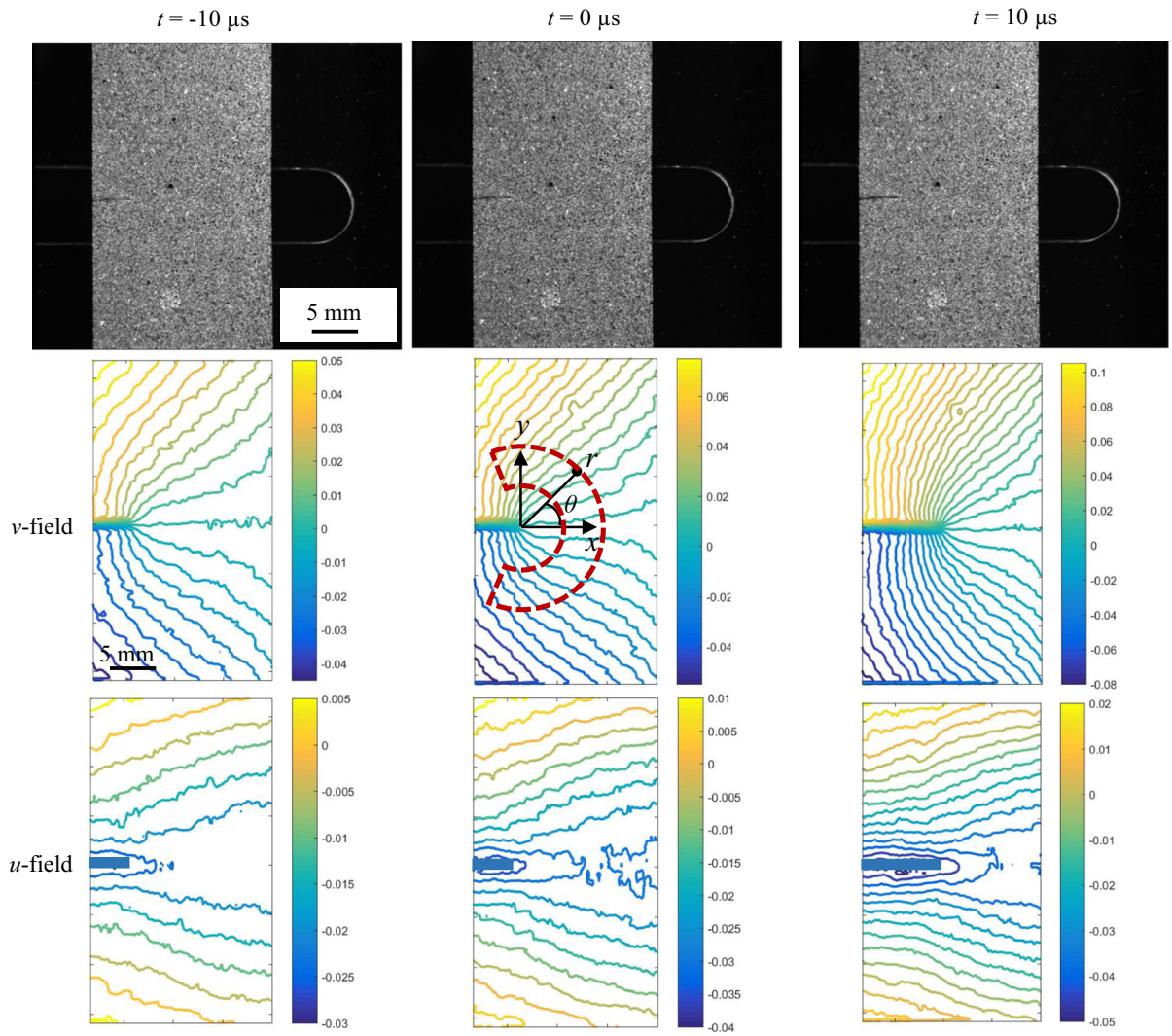

Fig. 4 Speckle images (top row) with corresponding measured crack-opening displacement contours (middle row) and crack-sliding displacement contours (bottom row) for dynamic fracture of F-CNP. Contours are shown in 10 μm increments and the color bar scale is in mm. See "Supplementary materials"

shape in case of the *u*-field and magnitude in case of the *v*-field relative to the initial crack.

The crack tip position from crack-opening displacement contours were identified from each of the images. Subsequently, the crack velocity histories for F-CNP samples were obtained via the finite difference scheme and are shown in Fig. 5 for two separate tests. It can be observed that the velocity histories essentially overlap on each other, indicating rather good repeatability of these experimental results. The crack velocities increase from 0 to ∼550 m/s in ∼10 μs after crack initiation and then become relatively steady at ∼660 m/s, which is equal to ∼35% C_R (Rayleigh wave speed based on the measured elastic modulus, Poisson's ratio and mass density).

The surface features of F-CNP were examined during fracture in real-time with the aid of ultrahigh-speed photography on a third specimen without decorating it speckles. That is, the dynamic fracture on a F-CNP sample without speckles was repeated by focusing the camera on the surface directly to see details near the crack tip vicinity during dynamic crack propagation. Three selected real-time images are shown in the top row of Fig. 6 (please see

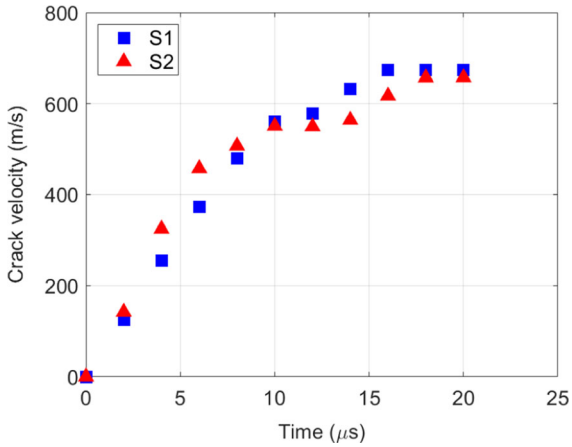

Fig. 5 Measured crack velocities for two dynamically loaded F-CNP specimens

"Supplementary materials" for video). In these images, $t = -30\mu s$ corresponds to the state before the specimen experiences dynamic loading, hence, no deformation at the original crack tip can be discerned. The $t = 0\mu s$ image corresponds to the time instant one frame before crack initiation at the original crack tip. In this image, a whitened zone ahead and around the crack tip can be clearly observed. During crack propagation, the whitened zone also appears along the two crack flanks seen at the time instant $t = 14\mu s$. It can be also found that the whitened zone at $t = 0\mu s$ appears wider than that the one at $t = 14\mu s$, attributable to the development of an inelastic deformation zone within which CNFs are pulled apart prior to crack initiation. The whitened zone ahead of the crack tip during the crack propagation is relatively long and narrow, potentially due to the combined effects of bridged fibers behind the crack tip and stretched fibers ahead of crack tip. These could contribute to the enhancement of crack growth resistance. The edges of this fractured specimen were observed using a Keyence VHX-6000 series digital microscope, and a representative image is shown in bottom row of Fig. 6. It is evident that the whitened zone appears along the crack path. This craze-like appearance, similar to the one often seen in many engineering polymers, could contribute to resistance of the material to crack growth through inelastic deformations. A similar phenomenon is also observed during fracture of CNF reinforced hydrogels (Yang et al. 2019).

Extraction of stress intensity factors (SIFs)

The stress intensity factor (SIF) histories were calculated using an over-deterministic least-squares

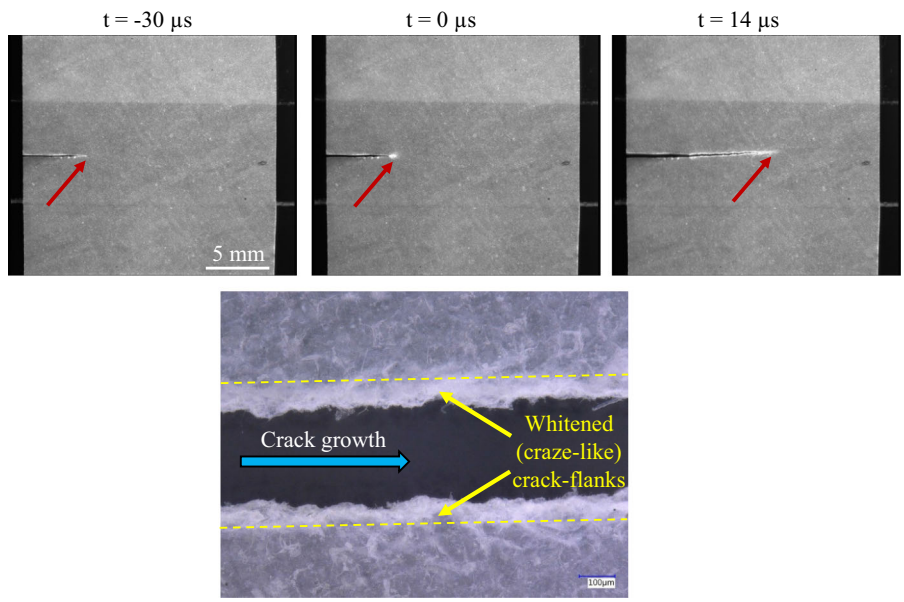

Fig. 6 (Top-row) Images of dynamic crack tip (denoted by the red arrow) propagation in F-CNP sample showing whitened zone. (Bottom) Micrograph of fractured specimen edges showing whitened crack flanks (blue arrow indicates the crack growth direction). See "Supplementary materials"

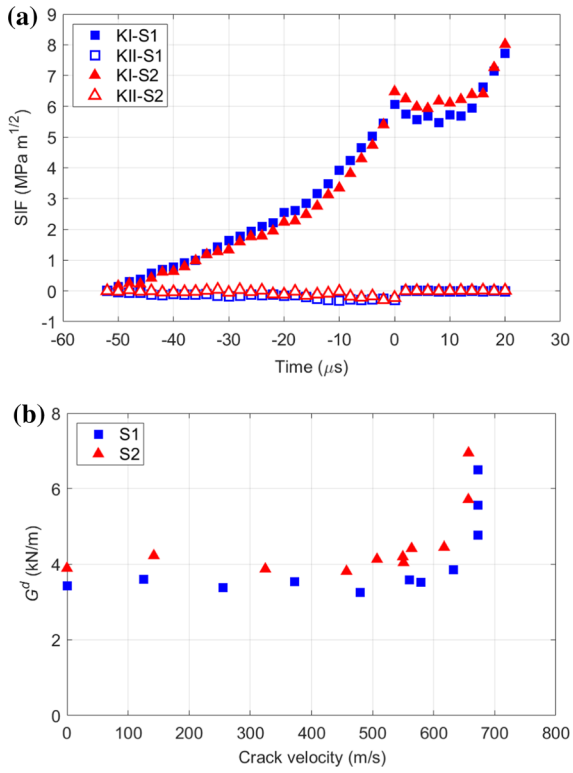

Fig. 7 Dynamic fracture parameters for two F-CNP specimens: (**a**) Measured stress intensity factor (SIF) histories, $t = 0$ corresponds to crack initiation; (**b**) Variation of dynamic strain energy release rates with crack velocity

analysis of crack-opening displacement contours, $v(x, y)$, measured by DIC. The asymptotic expression for the v-field around the dynamically propagating crack-tip can be expressed as (Nishioka and Atluri 1983; Jajam et al. 2013):

$$v(r,\theta) = \sum_{n=1}^{N} \frac{(K_I)_n B_I(V)}{2\mu}\sqrt{\frac{2}{\pi}}(n+1)\left\{-\beta_1 r_1^{\frac{n}{2}}\sin\frac{n}{2}\theta_1 + \frac{h(n)}{\beta_2} r_2^{\frac{n}{2}}\sin\frac{n}{2}\theta_2\right\} + \sum_{n=1}^{N}\frac{(K_{II})_n B_{II}(V)}{2\mu}\sqrt{\frac{2}{\pi}}(n+1)\left\{\beta_1 r_1^{\frac{n}{2}}\cos\frac{n}{2}\theta_1 + \frac{h(\overline{n})}{\beta_2} r_2^{\frac{n}{2}}\cos\frac{n}{2}\theta_2\right\} \quad (1)$$

where v is the crack-opening displacement, (r, θ) denotes the crack-tip polar coordinates as shown in Fig. 4. The discrete v-field data in the region around the crack-tip, $3\text{ mm} \le r \le 6\text{ mm}$, $-120° \le \theta \le 120°$, was used in the analysis to minimize the uncertainty associated with the precise crack-tip location yet sufficiently close to the crack-tip. In Eq. (1), $(K_I)_1 = K_I$ and $(K_{II})_1 = K_{II}$ denote the mode-I and mode-II SIFs, respectively, $r_m = \sqrt{x^2 + \beta_m^2 y^2}$, $\theta_m = \tan^{-1}\left(\frac{\beta_m y}{x}\right)$, $m = 1, 2$, $\beta_1 = \sqrt{1 - \left(\frac{V}{C_l}\right)^2}$, $\beta_2 = \sqrt{1 - \left(\frac{V}{C_s}\right)^2}$, $C_l = \sqrt{\frac{(\kappa+1)\mu}{(\kappa-1)\rho}}$, $C_s = \sqrt{\frac{\mu}{\rho}}$, $\kappa = \frac{3-\upsilon}{1+\upsilon}$ for plane stress, V, μ, ρ, υ are the crack velocity, shear modulus, mass density and Poisson's ratio of F-CNP, respectively. The remaining functions in Eq. (1) are defined as,

$h(n) = \frac{2\beta_1\beta_2}{1+\beta_2}$ for $n =$ odd, $h(n) = \frac{1+\beta_2^2}{2}$ for $n =$ even and $h(\overline{n}) = h(n+1)$;

$B_I(V) = \frac{1+\beta_2^2}{D}, B_{II}(V) = \frac{2\beta_2}{D}, D = 4\beta_1\beta_2 - \left(1+\beta_2^2\right)^2$.

In the above equation, the effect of non-singular far-field deformations, if any, on the measured K_I and K_{II} was offset by using four higher order terms ($N = 4$) while performing least-squares analysis. It should also be noted that the crack-tip displacements were forced to be zero during the analysis.

The measured crack velocities, V and SIFs were used to calculate the dynamic energy release rates for dynamically growing cracks using (Ravi-Chandar 2004):

$$G^d = \frac{1}{E}\left[A_I(V)K_I^2 + A_{II}(V)K_{II}^2\right] \quad (2)$$

where $A_I(V) = \frac{V^2\beta_1}{(1-\upsilon)C_s^2 D}$, $A_{II}(V) = \frac{V^2\beta_2}{(1-\upsilon)C_s^2 D}$.

Results and discussion

Dynamic fracture

The dynamic SIFs calculated from Eq. (1) are plotted for two specimens in Fig. 7a. The time axis of these plots was shifted so that $t = 0$ corresponds to crack initiation at the original edge crack-tip. The solid and open symbols represent SIFs, K_I and K_{II}, respectively. The K_I histories increase monotonically for both specimens, almost linearly in the beginning, until crack initiation. The dynamic fracture toughness (K_I at $t = 0$) was recorded at 6.3 ± 0.3 MPa m$^{1/2}$. The time rate of change of K_I, or $\frac{dK_I}{dt}$, was $\sim(4.3 \pm 1.6) \times 10^5$ MPa m$^{1/2}$/s at crack initiation based on a few data points in the K_I history just prior to initiation. It can be observed that there is a drop in the K_I histories

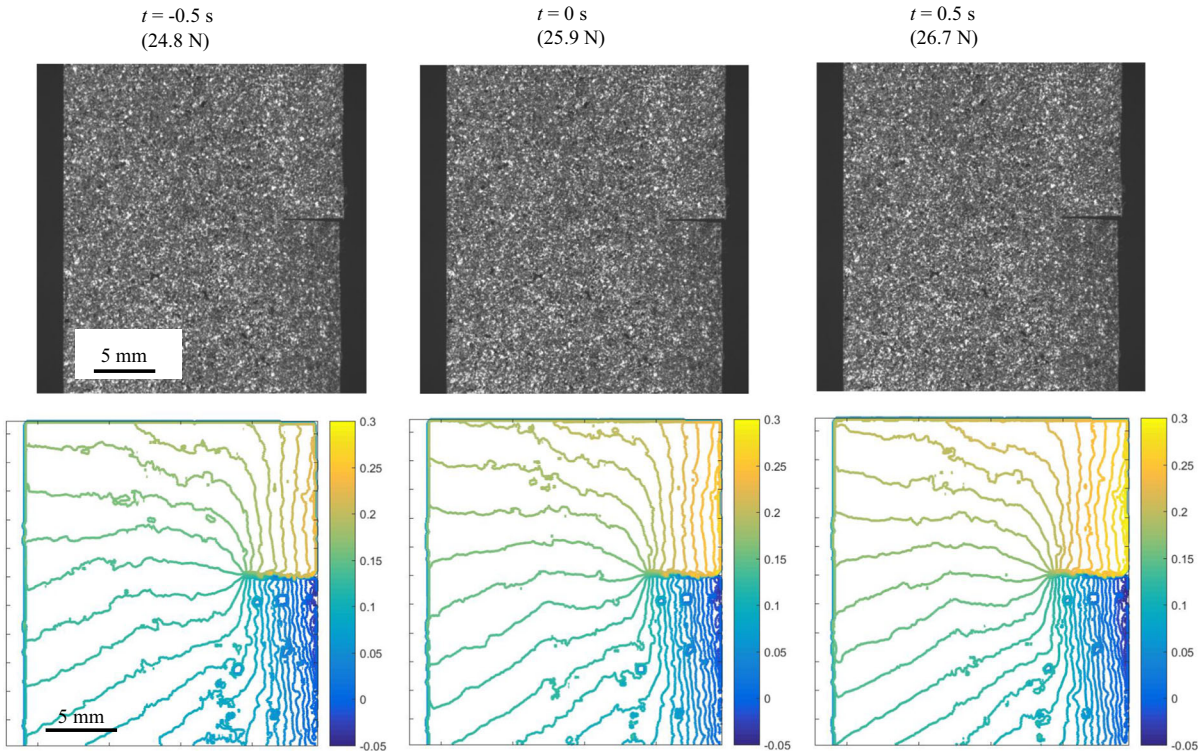

Fig. 8 Speckle images (top row) with corresponding measured crack-opening displacement contours (bottom row) for quasi-static fracture of F-CNP. Contours are shown in 10 μm increments and the color bar scale is in mm

immediately after crack initiation to ∼5.6 MPa $m^{1/2}$, which is due to dynamic unloading following crack initiation from the stationary tip. Microscale fiber bridging and blunting[1] at the stationary notch tip also contribute to this behavior. Subsequently, the K_I histories increase monotonically again due to velocity effects as well as craze-like crack flank whitening behavior until the end of the observation window, as shown in Fig. 6. The fiber bridging and tortuous crack path effectively increases the resistance to crack growth. The K_{II} histories throughout the observation window are nearly zero, in both the pre- and post-crack initiation regimes, due to the occurrence of a nominally mode-I fracture. The nonzero values of K_{II} are useful to assess potential errors in the least-squares analysis and/or crack tip location errors during data analysis. The two sets of experimental results for two different specimens agree with each other very well indicating good reproducibility of these experiments.

The dynamic SIFs are a function of crack velocity and loading rate $\left(\frac{dK_I}{dt}\right)$ (Ravi-Chandar 2004). Accordingly, using measured crack velocities V in Fig. 5 and post-initiation stress intensity factors K_I and K_{II} in Fig. 7a, the dynamic energy release rates (G^d) for growing cracks were evaluated from Eq. (2). The results are plotted in Fig. 7b. It can be observed that the measured value of G^d is ∼3.7 kN/m at crack initiation. After crack initiation, $G^d(V)$ is nearly a constant initially, ranging between ∼3.4 and ∼4.4 kN/m, until crack velocity reaches ∼620 m/s. Later on, the G^d values dramatically increase (to ∼7 kN/m within the observation window) in what appears to be a narrow terminal velocity range of 620–670 m/s for this material.

Comparison with quasi-static fracture behavior

The quasi-static fracture of F-CNP single edge-notched (SEN) specimens subjected to uniaxial

[1] Based on the nominal values of critical stress intensity factor (∼6.3 MPam), yield stress (∼50 MPa) and elastic modulus (∼10.5 GPa), the estimated critical crack tip opening displacement under plane stress conditions is ∼90 μm, higher than the initial notch tip root radius suggesting blunting.

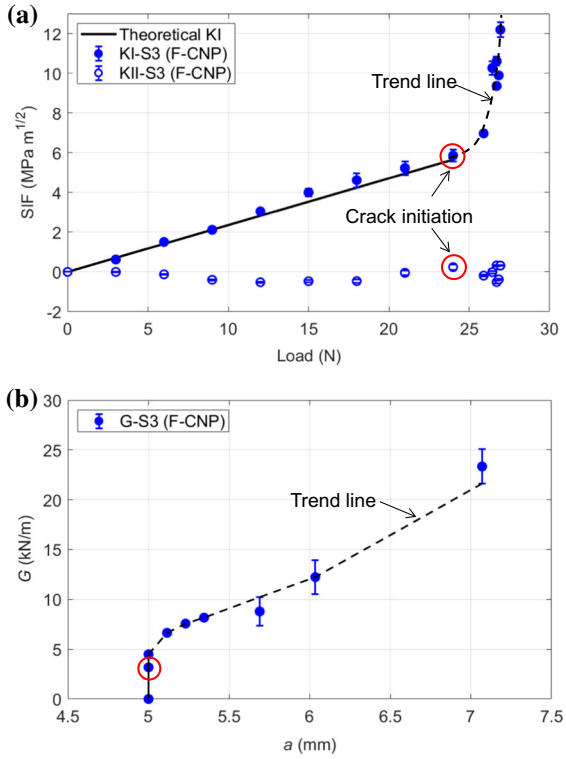

Fig. 9 Fracture parameters for F-CNP subjected to quasi-static fracture: (**a**) Measured stress intensity factor (SIF) histories at different loads levels; (**b**) Strain energy release rates in the post-crack initiation regime. Solid line indicates values before crack initiation, dotted line indicates unstable crack growth

tension was investigated by the authors in a previous study (Miao et al. 2020). Those results are compared with the dynamic counterparts to infer the loading rate effects. The experimental details are intentionally not included here for the sake of brevity and the readers can find those details in Ref. (Miao et al. 2020).

The speckle images and the related crack-opening displacement contours (v-field) for a few select time instants are shown in Fig. 8. In these plots, $t = 0$ s corresponds to the recorded image just before crack initiation. The specimen here was also subjected to mode-I loading conditions and hence contours in v-field displacements are nominally symmetric in shape and magnitude relative to the crack. However, when compared to the v-field contours for the dynamic fracture cases shown in Fig. 4, there is more noise in these contours due to the rigid body motions that are essentially negligible during dynamic fracture event due to the short observation window of approx. 80 microseconds. Furthermore, the displacement contours behind the crack-tip show asymmetry; that is, more contours on the lower half of the specimen relative to the upper half. Tests on other specimens have also produced similar results despite exercising care to eliminate misalignment. This suggests a failure mechanism unique to F-CNP that produces an out-of-plane deflection of crack flanks due to fiber entanglement. This in turn causes antisymmetric but pseudo crack opening displacements in addition to the actual mode-I deformations. The crack opening displacement contours ahead of the crack, however, remain unaffected and follow expected trends of a mode-I crack and hence can be analyzed (Miao et al. 2020).

The measured v-field results from DIC for one representative specimen (#S3) subjected to quasi-static loading were used to calculate the SIFs in both

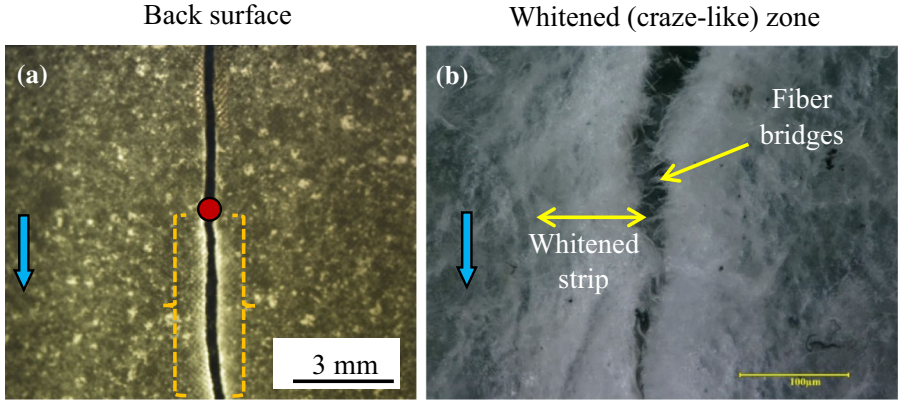

Fig. 10 Quasi-static crack growth features for F-CNP: (**a**) Image of back surface of F-CNP. (**b**) Micrographs of fractured specimen edges close to the crack tip. The blue arrow indicates the crack growth direction, and the red dot is the initial notch tip

the pre- and post-crack initiation regimes. The mode-I SIFs in the pre-crack initiation regime were comparatively examined relative to the theoretical counterparts based on the measured load history at 3 N intervals until crack initiation. The comparison between these two is shown in Fig. 9a. The solid and open symbols represent K_I and K_{II}, respectively. The solid line corresponds to the theoretical values. It can be observed from the plot that the quasi-static fracture toughness for F-CNP is $\sim$5.9 MPa m$^{1/2}$. The loading rate assessed in terms of time rate of change of K_I, or $\frac{dK_I}{dt}$, is $\sim(6 \pm 0.5) \times 10^{-1}$ MPa m$^{1/2}$/s at crack initiation based on a few data points in the K_I history leading up to initiation. It is evident in Fig. 9a that there is a good agreement between the experimental and theoretical values of mode-I SIF from linear elastic fracture mechanics. It should be noted here that the fracture toughness value of F-CNP is at least 50% higher than that for polycarbonate (PC), a tough engineering polymer known for its superior ductility and fracture toughness. The mode-I SIFs in the post-crack initiation regime are also plotted in Fig. 9a and they increase dramatically, up to 12 MPa m$^{1/2}$, suggesting that F-CNP, a natural biopolymer, is capable of offering highly desirable crack growth resistance during crack growth. The mode-II SIF values are also plotted for completeness even though the loading was nominally mode-I. The non-zero and negligibly small values of K_{II} help provide error estimates due to least-squares analysis approach of extracting SIFs.

To quantify the crack growth resistance characteristic of F-CNP noted above, the strain energy release rate (G) was evaluated using the SIFs in the post-crack initiation regime. Knowing the crack length at each load level, plots of G vs. a (crack length), or the so-called crack growth resistance curve, was obtained and is shown in Fig. 9b. It can be observed that values of G for F-CNP increase from $\sim$3.2 kN/m at initiation to $\sim$23.3 kN/m towards the end of the observation window. Again, this increasing trend of G displays a desirable resistance to crack growth of F-CNP.

The fractography of F-CNP subjected to quasi-static fracture performed using an optical microscope and is shown in Fig. 10a. A narrow strip of whitened region relative to the surroundings, marked by yellow braces in the figure, was observed along the two crack flanks on the specimens. These fractured edges were also observed using Keyence VHX-6000 series digital microscope and is shown in Fig. 10b. A highly tortuous crack path among the entangled fibers in the whitened region suggest fracture toughening. The similar whitened zone was also observed in the dynamic fracture counterpart shown in Fig. 6. However, it should be noted here that fractography in the quasi-static counterpart revealed the occurrence of the whitened zone only in the wake of the crack.

The measured fracture toughness of $\sim$6.3 MPa m$^{1/2}$ under dynamic loading conditions ($\left(\frac{dK_I}{dt}\right) \sim 4.3 \times 10^5$ - MPa m$^{1/2}$/s) is slightly higher than $\sim$5.9 MPa m$^{1/2}$ from quasi-static ($\left(\frac{dK_I}{dt}\right) \sim 6 \times 10^{-1}$ MPa m$^{1/2}$/s) experiments. It should be noted that this increase for a low density (1225 kg/m^3) fibrous biodegradable natural material with a relatively high elastic modulus (10 GPa) is unlike those evident in conventional composites. (That is, the behavior is contrary to fiber reinforced composites which often show lower fracture toughness under dynamic loading conditions relative to the quasi-static counterparts (Miao and Tippur 2019) in matrix dominant orientations.) Furthermore, the crack initiation toughness of F-CNP is significantly higher than tough engineering polymers such as polycarbonate, for which the reported fracture toughness is in the range 3–4 MPa m$^{1/2}$ with a significantly lower elastic modulus of $\sim$2.5 GPa under quasi-static conditions and $\sim$2.0 MPa m$^{1/2}$ under dynamic conditions (Sundaram and Tippur 2017). These suggest a clear superiority of F-CNP in terms of fracture behavior under both quasi-static and dynamic loading conditions.

In the post-crack initiation regime, the increase of strain energy release rate is approximately seven-fold, starting from $\sim$3.2 to $\sim$23.3 kN/m, in the observation window under quasi-static conditions. Under dynamic conditions, the energy release rates also show a rapid increase from $\sim$3.4 to $>$ 7 kN/m as the crack speed reaches terminal speed in the 620–670 m/s range. Thus, F-CNP shows increasing crack growth resistance in both quasi-static and dynamic loading conditions and at two vastly different loading rates, indicating superior fracture behavior during crack growth. The postmortem examination and fractography of crack flanks suggest that the crack growth resistance is primarily due to the formation of whitened strips evident all along the crack path. The synergistic effects of bridged fibers across the crack faces, microscale tortuosity in the crack path and fiber

pull-outs ahead of the crack tip increase the resistance of F-CNP to crack growth. It is well-known that under dynamic conditions, material ductility in case of polymers (Sundaram and Tippur 2017) and microcracking ahead of crack tip in case of brittle materials (Miao and V Tippur 2020), are common sources of crack growth resistance. Thus, the observed toughening in F-CNP is in some ways different from these well-known situations, which indicates the uniqueness of crack growth characteristics in F-CNP.

Concluding remarks

Dynamic fracture behaviors of filtered cellulose nanopaper (F-CNP) are experimentally studied in this work using 2D-DIC along with ultrahigh-speed photography. The dynamic loading of F-CNP is achieved by a specially devised acrylic holder with a wide precut slot bridged by a CNP strip with an edge crack. The crack opening displacements measured from DIC are used to calculate the fracture parameters in the entire fracture process. The results of quasi-static fracture behavior of F-CNP are also included here to comparatively show the loading rate effects. The high fracture toughness and the increasing crack growth resistance during crack propagation suggest the superior fracture characteristics of F-CNP for promising engineering applications.

Acknowledgments Haishun Du acknowledges the financial support from the China Scholarship Council (No. 201708120052).

Declarations

Conflict of interest There is no conflict of interest.

Ethical approval This article does not contain any studies with human participants or animals performed by any of the authors.

References

Benítez AJ, Walther A (2017) Cellulose nanofibril nanopapers and bioinspired nanocomposites: a review to understand the mechanical property space. J Mater Chem A 5:16003–16024. https://doi.org/10.1039/c7ta02006f

Chen Y, Zhang L, Mei C et al (2020) Wood-inspired anisotropic cellulose nanofibril composite sponges for multifunctional applications. ACS Appl Mater Interf. https://doi.org/10.1021/acsami.0c10645

Chu TC, Ranson WF, Sutton MA (1985) Applications of digital-image-correlation techniques to experimental mechanics. Exp Mech 25:232–244. https://doi.org/10.1007/BF02325092

Diaz JA, Wu X, Martini A et al (2013) Thermal expansion of self-organized and shear-oriented cellulose nanocrystal films. Biomacromol 14:2900–2908. https://doi.org/10.1021/bm400794e

Du H, Liu W, Zhang M et al (2019) Cellulose nanocrystals and cellulose nanofibrils based hydrogels for biomedical applications. Carbohydr Polym 209:130–144. https://doi.org/10.1016/J.CARBPOL.2019.01.020

Du H, Parit M, Wu M et al (2020) Sustainable valorization of paper mill sludge into cellulose nanofibrils and cellulose nanopaper. J Hazard Mater 400:123106. https://doi.org/10.1016/j.jhazmat.2020.123106

Du H, Parit M, Liu K et al (2021) Engineering cellulose nanopaper with water resistant, antibacterial, and improved barrier properties by impregnation of chitosan and the followed halogenation. Carbohydr Polym 270:118372. https://doi.org/10.1016/j.carbpol.2021.118372

Du H, Zhang M, Liu K et al (2022) Conductive PEDOT:PSS/cellulose nanofibril paper electrodes for flexible supercapacitors with superior areal capacitance and cycling stability. Chem Eng J 428:131994. https://doi.org/10.1016/j.cej.2021.131994

Jajam KC, Bird SA, Auad ML, Tippur HV (2013) Tensile, fracture and impact behavior of transparent Interpenetrating polymer networks with polyurethane-poly(methyl methacrylate). Polym Test 32:889–900. https://doi.org/10.1016/J.POLYMERTESTING.2013.04.010

Jung YH, Chang TH, Zhang H et al (2015) High-performance green flexible electronics based on biodegradable cellulose nanofibril paper. Nat Commun. https://doi.org/10.1038/ncomms8170

Kargarzadeh H, Huang J, Lin N et al (2018) Recent developments in nanocellulose-based biodegradable polymers, thermoplastic polymers, and porous nanocomposites. Prog Polym Sci 87:197–227. https://doi.org/10.1016/J.PROGPOLYMSCI.2018.07.008

Kirugulige MS, Tippur HV, Denney TS (2007) Measurement of transient deformations using digital image correlation method and high-speed photography: application to dynamic fracture. Appl Opt 46:5083–5096. https://doi.org/10.1364/AO.46.005083

Lee D, Tippur H, Bogert P (2010) Quasi-static and dynamic fracture of graphite/epoxy composites: an optical study of loading-rate effects. Compos Part B Eng 41:462–474. https://doi.org/10.1016/J.COMPOSITESB.2010.05.007

Lee KY, Aitomäki Y, Berglund LA et al (2014) On the use of nanocellulose as reinforcement in polymer matrix composites. Compos Sci Technol 105:15–27. https://doi.org/10.1016/j.compscitech.2014.08.032

Liu W, Du H, Zhang M et al (2020) Bacterial cellulose-based composite scaffolds for biomedical applications: a review. ACS Sustain Chem Eng 8:7536–7562. https://doi.org/10.1021/acssuschemeng.0c00125

Liu H, Du H, Zheng T et al (2021) Cellulose based composite foams and aerogels for advanced energy storage devices.

Chem Eng J 426:130817. https://doi.org/10.1016/j.cej.2021.130817
Mao R, Goutianos S, Tu W et al (2017) Comparison of fracture properties of cellulose nanopaper, printing paper and buckypaper. J Mater Sci 52:9508–9519. https://doi.org/10.1007/s10853-017-1108-4
Meng Q, Li B, Li T, Feng X-Q (2017) A multiscale crack-bridging model of cellulose nanopaper. J Mech Phys Solids 103:22–39. https://doi.org/10.1016/J.JMPS.2017.03.004
Meng Q, Li B, Li T, Feng XQ (2018) Effects of nanofiber orientations on the fracture toughness of cellulose nanopaper. Eng Fract Mech 194:350–361. https://doi.org/10.1016/j.engfracmech.2018.03.034
Miao C, Tippur HV (2019) Fracture behavior of carbon fiber reinforced polymer composites: an optical study of loading rate effects. Eng Fract Mech. https://doi.org/10.1016/j.engfracmech.2018.12.035
Miao C, Tippur HV (2020) Dynamic fracture of soda-lime glass plates studied using two modified digital gradient sensing techniques. Eng Fract Mech 232:107048. https://doi.org/10.1016/j.engfracmech.2020.107048
Miao C, Du H, Parit M et al (2020) Superior crack initiation and growth characteristics of cellulose nanopapers. Cellulose. https://doi.org/10.1007/s10570-020-03015-x
Nishioka T, Atluri SN (1983) Path-independent integrals, energy release rates, and general solutions of near-tip fields in mixed-mode dynamic fracture mechanics. Eng Fract Mech 18:1–22. https://doi.org/10.1016/0013-7944(83)90091-7
Nogi M, Karakawa M, Komoda N et al (2015) Transparent conductive nanofiber paper for foldable solar cells. Sci Rep 5:1–7. https://doi.org/10.1038/srep17254
Pan B, Qian K, Xie H, Asundi A (2009) Two-dimensional digital image correlation for in-plane displacement and strain measurement: a review. Meas Sci Technol 20:062001. https://doi.org/10.1088/0957-0233/20/6/062001
Parit M, Aksoy B, Jiang Z (2018) Towards standardization of laboratory preparation procedure for uniform cellulose nanopapers. Cellulose 25:2915–2924. https://doi.org/10.1007/s10570-018-1759-6
Parit M, Du H, Zhang X et al (2020) Polypyrrole and cellulose nanofiber based composite films with improved physical and electrical properties for electromagnetic shielding applications. Carbohydr Polym 240:116304. https://doi.org/10.1016/j.carbpol.2020.116304
Ravi-Chandar K (2004) Dynamic fracture. Elsevier, San Diego
Sundaram BM, Tippur HV (2017) Dynamic mixed-mode fracture behaviors of PMMA and polycarbonate. Eng Fract Mech 176:186–212. https://doi.org/10.1016/J.ENGFRACMECH.2017.02.029
Sutton MA, Orteu J-J, Schreier H (2009) Image correlation for shape, motion and deformation measurements: basic concepts, theory and applications, 1st edn. Springer Publishing Company, Incorporated
Wang Q, Du H, Zhang F et al (2018) Flexible cellulose nanopaper with high wet tensile strength, high toughness and tunable ultraviolet blocking ability fabricated from tobacco stalk: via a sustainable method. J Mater Chem A 6:13021–13030. https://doi.org/10.1039/c8ta01986j
Wu J, Che X, Hu H-C et al (2020a) Organic solar cells based on cellulose nanopaper from agroforestry residues with an efficiency of over 16% and effectively wide-angle light capturing. J Mater Chem A 8:5442–5448. https://doi.org/10.1039/C9TA14039E
Wu M, Sukyai P, Lv D et al (2020b) Water and humidity-induced shape memory cellulose nanopaper with quick response, excellent wet strength and folding resistance. Chem Eng J 392:123673. https://doi.org/10.1016/j.cej.2019.123673
Wyss CS, Karami P, Bourban P-E, Pioletti DP (2018) Cyclic loading of a cellulose/hydrogel composite increases its fracture strength. Extrem Mech Lett 24:66–74. https://doi.org/10.1016/J.EML.2018.09.002
Xie H, Du H, Yang X, Si C (2018) Recent strategies in preparation of cellulose nanocrystals and cellulose nanofibrils derived from raw cellulose materials. Int J Polym Sci. https://doi.org/10.1155/2018/7923068
Xing J, Tao P, Wu Z et al (2019) Nanocellulose-graphene composites: a promising nanomaterial for flexible supercapacitors. Carbohydr Polym 207:447–459. https://doi.org/10.1016/j.carbpol.2018.12.010
Yang J, Shao C, Meng L (2019) Strain rate-dependent viscoelasticity and fracture mechanics of cellulose nanofibril composite hydrogels. Langmuir 35:10542–10550. https://doi.org/10.1021/acs.langmuir.9b01532
Yoneyama S, Morimoto Y, Takashi M (2006) Automatic evaluation of mixed-mode stress intensity factors utilizing digital image correlation. Strain 42:21–29. https://doi.org/10.1111/j.1475-1305.2006.00246.x
Zhao M, Ansari F, Takeuchi M et al (2018) Nematic structuring of transparent and multifunctional nanocellulose papers. Nanoscale Horiz 3:28–34. https://doi.org/10.1039/c7nh00104e
Zhu H, Zhu S, Jia Z et al (2015) Anomalous scaling law of strength and toughness of cellulose nanopaper. Proc Natl Acad Sci 112:8971–8976. https://doi.org/10.1073/PNAS.1502870112